
This copy is for your personal, non-commercial use only.

If you wish to distribute this article to others, you can order high-quality copies for your colleagues, clients, or customers by [clicking here](#).

Permission to republish or repurpose articles or portions of articles can be obtained by following the guidelines [here](#).

The following resources related to this article are available online at www.sciencemag.org (this information is current as of April 24, 2014):

Updated information and services, including high-resolution figures, can be found in the online version of this article at:

<http://www.sciencemag.org/content/344/6182/420.full.html>

Supporting Online Material can be found at:

<http://www.sciencemag.org/content/suppl/2014/04/23/344.6182.420.DC1.html>

A list of selected additional articles on the Science Web sites **related to this article** can be found at:

<http://www.sciencemag.org/content/344/6182/420.full.html#related>

This article **cites 41 articles**, 12 of which can be accessed free:

<http://www.sciencemag.org/content/344/6182/420.full.html#ref-list-1>

This article has been **cited by** 1 articles hosted by HighWire Press; see:

<http://www.sciencemag.org/content/344/6182/420.full.html#related-urls>

This article appears in the following **subject collections**:

Neuroscience

<http://www.sciencemag.org/cgi/collection/neuroscience>

27. R. D. Barrett, D. Schluter, *Trends Ecol. Evol.* **23**, 38–44 (2008).
28. A. D. Barton, S. Dutkiewicz, G. Flierl, J. Bragg, M. J. Follows, *Science* **327**, 1509–1511 (2010).
29. F. Rodriguez-Valera et al., *Nat. Rev. Microbiol.* **7**, 828–836 (2009).
30. C. C. Thompson et al., *Microb. Ecol.* **66**, 752–762 (2013).

Acknowledgments: We thank S. Itzkovitz, P. H. R. Calil, D. Sher, R. Milo, P. M. Berube, A. P. Yelton, R. Braakman, and particularly M. F. Polz for comments on the manuscript. We thank the Bermuda Atlantic Time-series Study for sample collection, the Bigelow Laboratory Single Cell Genomics Center for single-cell sorting and whole-genome amplification, and

the BioMicroCenter facility at MIT for their contributions to the generation of genomic data. N.K. acknowledges the Rothschild Foundation (Yad Hanadiv) and the National Oceanic and Atmospheric Administration “Climate and Global Change” Postdoctoral Research Fellowships. This work was supported by grants to S.W.C. from the NSF Evolutionary Biology Section and Biological Oceanography Section, the NSF Center for Microbial Oceanography Research and Education (C-MORE), the U.S. Department of Energy (DOE)–GTL, and the Gordon and Betty Moore Foundation Marine Microbiology Initiative; to R. Stepanauskas from the NSF Biological Oceanography Section; and to R.R.M. from the DOE (contract number DE-AC02-05CH11231). Genomic data have been deposited in National Center for Biotechnology

Information GenBank under accession numbers KJ477896 to KJ479276 and JFKN00000000 to JFOE00000000. Additional data files have been deposited to Dryad (doi:10.5061/dryad.9r0p6).

Supplementary Materials

www.sciencemag.org/content/344/6182/416/suppl/DC1
Materials and Methods
Figs. S1 to S21
Tables S1 to S13
References (31–91)
Data S1

18 November 2013; accepted 20 March 2014
10.1126/science.1248575

Structure-Guided Transformation of Channelrhodopsin into a Light-Activated Chloride Channel

Andre Berndt,^{1*} Soo Yeun Lee,^{1*} Charu Ramakrishnan,¹ Karl Deisseroth^{1,2,3†}

Using light to silence electrical activity in targeted cells is a major goal of optogenetics. Available optogenetic proteins that directly move ions to achieve silencing are inefficient, pumping only a single ion per photon across the cell membrane rather than allowing many ions per photon to flow through a channel pore. Building on high-resolution crystal-structure analysis, pore vestibule modeling, and structure-guided protein engineering, we designed and characterized a class of channelrhodopsins (originally cation-conducting) converted into chloride-conducting anion channels. These tools enable fast optical inhibition of action potentials and can be engineered to display step-function kinetics for stable inhibition, outlasting light pulses and for orders-of-magnitude-greater light sensitivity of inhibited cells. The resulting family of proteins defines an approach to more physiological, efficient, and sensitive optogenetic inhibition.

The microbial opsins (1–3) used for optical control of genetically targeted cellular activity (4–7) include light-activated proton and Cl[−] pumps and the cation channels called channelrhodopsins (ChRs). ChRs are derived from algae (3, 8–10) and, when expressed in neurons, can elicit precise action potential (AP) firing (11–15). ChRs conduct K⁺, Na⁺, protons, and Ca²⁺ (3, 10, 16, 17); because of this non-selective cation-conductance, ChRs display reversal potentials (V_{rev}) near 0 mV under physiological conditions and therefore depolarize neurons, leading to AP generation (18).

Direct light-triggered inhibition of neuronal activity is possible with inward-pumping Cl[−]-transporting opsins and outward-pumping proton-transporting opsins (10); hyperpolarization to −150 mV or beyond can be achieved (18–20). However, pumps are inefficient in neural systems because only one ion is moved per photon and no input resistance decrease is elicited (failing to recruit the most potent mechanism of spiking inhibition). Moreover, because the pumps use energy to transport ions against electrochemical gradients,

the creation of abnormal gradients is more likely (18). Last, pumps cannot take advantage of certain molecular engineering opportunities to achieve light sensitivity and long-term photocurrent stability enhanced by many orders of magnitude (but which depend on formation of a transmembrane pore) (21–23). Therefore, the creation of inhibitory channels has long been a central goal of optogenetics.

Given typical ion balance in neural systems, identification or creation of light-activated K⁺ or Cl[−] channels could give rise to inhibitory optogenetic tools. ChRs can be engineered to alter kinetics, spectrum, and selectivity among cations (10, 24, 25). However, V_{rev} has not been shifted sufficiently for nondepolarizing spike inhibition in neurons. We have designed a family of ChRs for Cl[−] permeability and capability to inhibit APs without depolarizing neurons to or beyond the AP-generation threshold.

Building on the high-resolution crystal structure of the ChR chimera C1C2 (24), we noted that the ion-selectivity pore of ChR is less ordered as compared with the well-defined symmetry of tetrameric K⁺-selective channels such as KcsA and NaK2K (26–31). Therefore, we speculated that the specific cation selectivity of ChR is rather a result of negative electrostatic potential surrounding the pore and vestibule; for instance, the C1C2 structure shows seven glutamates framing the conduction pathway (24). We hypothesized that sys-

tematic replacement of such residues within or close to the pore according to structure-guided electrostatic modeling could reverse this polarity and create an inhibitory ChR, if it were possible to maintain proper protein folding, membrane expression, optical activation, and pore gating.

We initiated a broad structure-guided screen by introducing single site-directed mutations into C1C2 (Fig. 1A). We expressed all variants in cultured rat hippocampal neurons and tested photocurrents using whole-cell patch-clamp so as to ensure proper function in neurons (external/internal [Cl[−]], 147 mM/4 mM). We quantified stationary photocurrent amplitudes across a range of holding potentials (Fig. 1B), with particular attention to V_{rev} , in order to identify permeability variants (Fig. 1C). C1C2 exhibits V_{rev} of −7 mV under these conditions, which is typical for nonspecific cation channels (16, 26, 32, 33). Certain mutations with powerful effects on V_{rev} displayed concomitant adverse effects on photocurrent sizes (such as E136R and E140K) (Fig. 1B), and were not studied further (34). More promising mutations, such as N297Q and H173R, exhibited both potent currents and altered V_{rev} (Fig. 1C) and were combined in a series of increasingly integrated mutations. The fivefold mutation T98S/E129S/E140S/E162S/T285N and fourfold mutation V156K/H173R/V281K/N297Q both displayed prominently-shifted V_{rev} (in the range of −40 mV) while maintaining functionality (Fig. 1, D and E).

We next combined these constructs to generate a ninefold mutated variant with contiguous shifts in expected electrostatic potential distribution (Fig. 2A and fig. S1) (24). We expressed the ninefold variant in human embryonic kidney (HEK) 293 cells to test both V_{rev} and permeability under controlled ion composition and optimized voltage clamp settings (Fig. 2B). We mapped photocurrents over a broad range of membrane potentials (Fig. 2C) (from −75 mV to +55 mV) (35). Under these conditions (external/internal [Cl[−]], 147mM/4mM), the combined ninefold mutation exhibited V_{rev} of −61 mV, which is far more negatively shifted than was the C1C2 backbone or either parental 4× or 5× construct (Fig. 2D). Despite this major change in functionality, both peak and stationary photocurrents remained fast and robust (predicting suitability for optogenetics, especially because this channel could also recruit a reduced-membrane resistance mechanism for spiking inhibition), and the original blue light-activation spectrum of C1C2

¹Department of Bioengineering, Stanford University, Stanford, CA 94305, USA. ²Department of Psychiatry and Behavioral Sciences, Stanford University, Stanford, CA 94305, USA. ³Howard Hughes Medical Institute, Stanford University, Stanford, CA 94305, USA.

*These authors contributed equally to this work.

†Corresponding author. E-mail: deissero@stanford.edu

was maintained, compared with the red-activation capability of the Cl⁻ pump eNpHR3.0 (thus maintaining a separable channel for inhibitory control in optogenetic applications) (Fig. 2E). We termed this ninefold variant “iC1C2.”

Because the shifted V_{rev} could be attributable to increased K⁺ selectivity or a new Cl⁻ conductance, we measured V_{rev} under varying ion compositions (corrected for the calculated junction potential arising from each condition) (35) in order to determine the specific ion selectivity of iC1C2. ChRs are highly permeable for protons and typically show no selectivity between K⁺ and Na⁺ (16). Therefore, with a pipette solution composition of 120 mM KCl at pH 7.3 and a bath solution of 120 mM NaCl also at pH 7.3, virtually no chemical gradient for permeant ions would be expected, and indeed, under these conditions V_{rev} for both C1C2 and iC1C2 was ~0 mV (Fig. 2F). Replacement of external KCl by CsCl would create a strong outward-directed gradient for K⁺ ions, and as expected under this condition, V_{rev} of C1C2 dropped to -17.4 mV, which is consistent with K⁺ as a major charge carrier. However, there was no such V_{rev} shift for iC1C2 (V_{rev} = -1 mV). These data do not support a hypothesis that iC1C2 achieves shifted V_{rev} through increased K⁺ conductance,

and in fact, iC1C2 does not appreciably conduct K⁺ under these conditions (Fig. 2F). To test the other possibility of new Cl⁻ conductivity, we replaced external Cl⁻ with gluconate (for a chemical Cl⁻ gradient of 8 mM_{ext}/128 mM_{int} and shifting its Nernst potential to +71 mV). Despite this strong outward-directed Cl⁻ gradient, C1C2 showed no shift in V_{rev} (0 mV), which was as expected because the native C1C2 does not conduct Cl⁻. In contrast, iC1C2 exhibited a positively shifted V_{rev} of +48 mV, revealing a strong contribution of Cl⁻ to the photocurrent (Fig. 2F). Last, we replaced internal Cl⁻ with gluconate to create a strong inward-directed Cl⁻ gradient (128 mM [Cl⁻]_{ext}/8 mM [Cl⁻]_{int}; $V_{Nernst-Cl}$ = -71 mV). The resulting V_{rev} was -6 mV for C1C2 but -57 mV for iC1C2, confirming a potent contribution from conducted Cl⁻ ions to iC1C2 photocurrents (Fig. 2G).

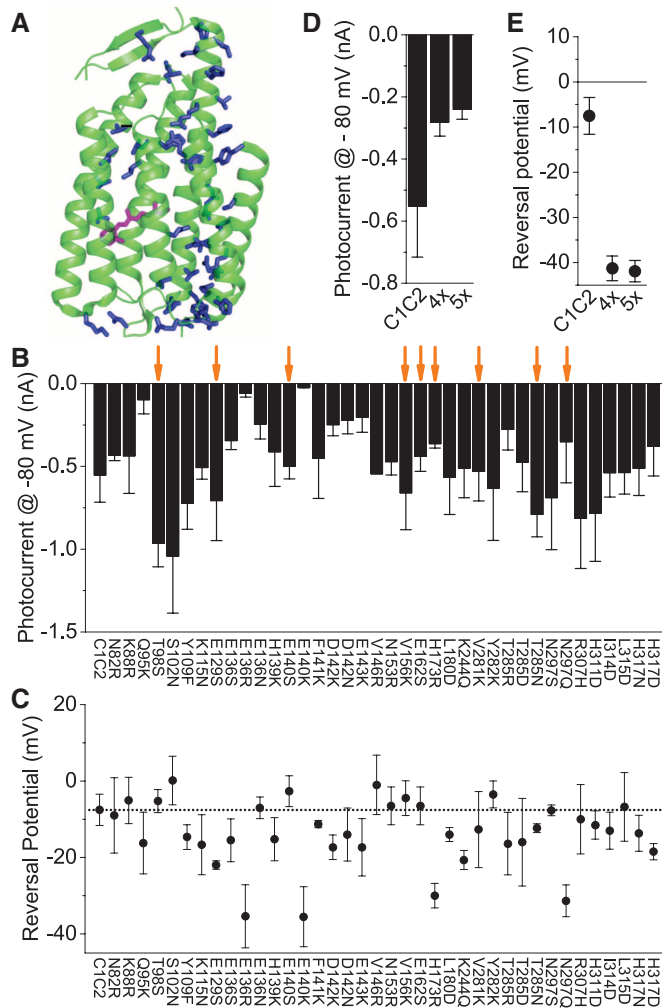
Because the V_{rev} for iC1C2 was not identical to the calculated $V_{Nernst-Cl}$, other ions such as protons (16) could be conducted as well. To explore this possibility in physiological Cl⁻ gradients, we altered the proton concentrations of internal and external solutions while maintaining the inward-directed Cl⁻ chemical gradient (128 mM_{ext}/8 mM_{int}; $V_{Nernst-Cl}$ = -71 mV) (Fig. 2H). We varied pH of external and internal solutions together (no proton

chemical gradient; $V_{Nernst-H^+}$ = 0 mV) and measured iC1C2 responses at physiological (7.3) and low (6.0) pH, with matched internal/external proton concentrations. We expected that at lower pH and more negative membrane potential, protons would contribute more to the iC1C2 photocurrent and thus positively shift V_{rev} toward the 0 mV Nernst potential for protons. Surprisingly, we found that the iC1C2 V_{rev} was more negatively shifted at pH 6 as compared with pH 7.3 (Fig. 2H), suggesting that iC1C2 conducts Cl⁻ even more robustly and maintains a prominently negative V_{rev} at lower pH values. Total iC1C2 photocurrents were greater at lower pH values (Fig. 2, I and J), which is consistent with a proton-enhanced Cl⁻ permeability. We calculated the ratio of Cl⁻ to proton permeability at the different pH values (α = P_{Cl}/P_H) (35). Indeed, at pH 6 the contribution of Cl⁻ to the overall current was 35 times higher than at pH 7.3, suggesting that even excursions to lower pH—as can happen during extreme neural activity—will not impair the important Cl⁻ conductance.

We next expressed C1C2 and iC1C2, each fused to enhanced yellow fluorescent protein (eYFP), in cultured hippocampal neurons (fig. S2). Mean resting potentials were not different (C1C2, -65 mV; iC1C2, -69 mV), and input resistances were in the expected range (above 200 megohms) for both constructs. We determined V_{rev} (Fig. 3A), which for iC1C2 (V_{rev} = -64 mV) was negatively shifted by 56 mV compared with C1C2 (V_{rev} = -7 mV) (Fig. 3B). This V_{rev} of iC1C2 lies more negative than the measured threshold for AP generation (V_{AP} = -55 mV) (Fig. 3C). Consequently, at V_{AP} in a voltage clamp C1C2 generated an inward-directed photocurrent of -475 pA, whereas iC1C2 produced an outward-directed photocurrent of +42 pA; in a current clamp, C1C2 depolarized neurons by +20 mV, whereas iC1C2 hyperpolarized neurons by -3 mV (Fig. 3D). In addition, input resistance dropped by ~50% during light in cells expressing iC1C2, indicating increased ion flux through membrane pores, and after light-off input resistance recovered to original levels (Fig. 3E).

The iC1C2 input-resistance effects and iC1C2 membrane polarization effects, that together would tend to maintain membrane potential below spike-firing threshold (Fig. 3F), suggested utility in optogenetic control of spiking. Indeed, optical activation of iC1C2 sufficed to inhibit electrically evoked spikes without exerting a depolarizing effect (Fig. 4, A to C). To further explore the properties of iC1C2, we mutated cysteine-167 to mimic step-function mutations of channelrhodopsin (21), which decelerate channel closure and extend lifetime of the ion-conducting state; as a result, brief light stimulation induces prolonged depolarization, and light sensitivity of cells expressing these variants is greatly increased (21–23). The inhibitory versions here define the SwiChR variants (for Step-waveform inhibitory ChR), including C167T (SwiChR_{CT}) and C167A (SwiChR_{CA}). We first expressed SwiChR_{CT} in HEK cells to determine channel kinetics and sensitivity. Both inward- and outward-directed photocurrents were

Fig. 1. Rational design and screen: V_{rev} -shifted ChRs. (A) C1C2 crystal structure [Protein Data Bank (PDB) 3UG9] (24), with residues used for screening in blue (retinal chromophore in magenta). (B) C1C2 mutations screened in neurons for photocurrent size at -80 mV (n = 6 to 8 cells). Arrows indicate nine mutations selected for C1C2_5x (T98S/E129S/E140S/E162S/T285N) and C1C2_4x (V156K/H173R/V281K/N297Q) constructs. (C) V_{rev} of C1C2 single-mutation constructs (n = 6 to 8 cells). (D) Comparison of photocurrent sizes for C1C2, C1C2_4x, and C1C2_5x. (E) Comparison of V_{rev} for C1C2, C1C2_4x, and C1C2_5x (n = 8 to 10 cells). Error bars indicate SEM.



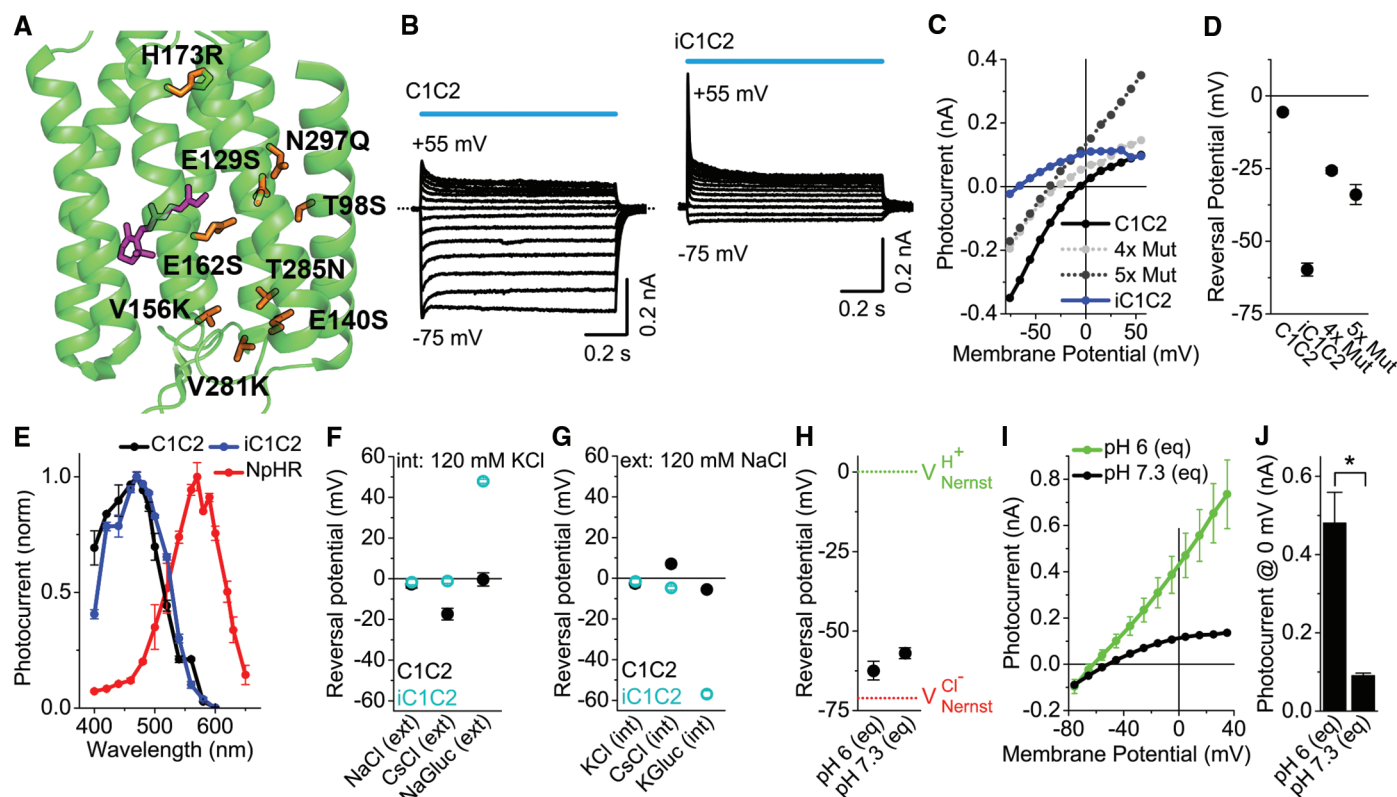
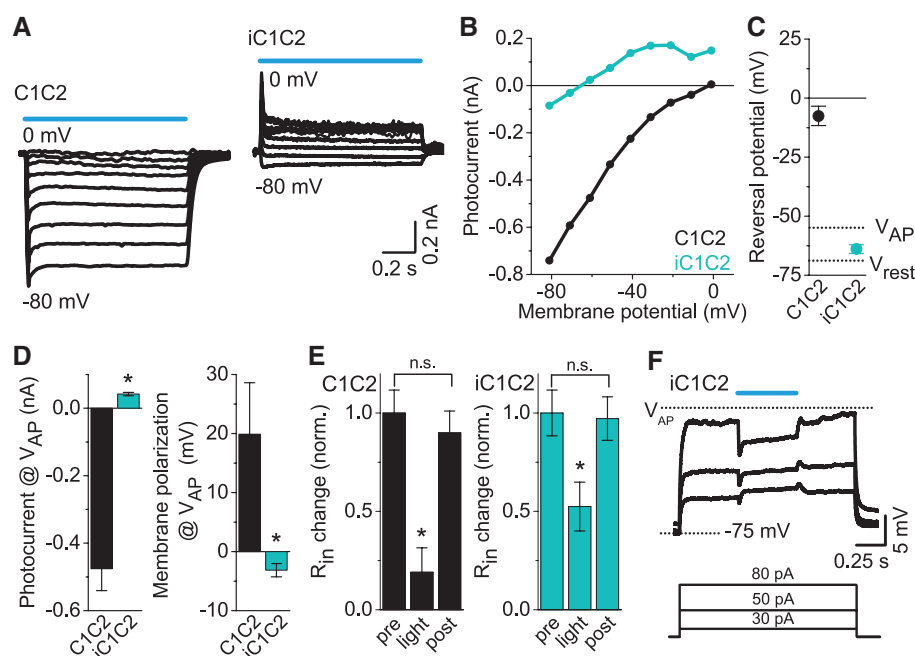


Fig. 2. iC1C2: biophysical properties. (A) C1C2 structure, with the nine residues mutated in C1C2_4x and C1C2_5x in orange. (B) Representative photocurrents and (C) corresponding current-voltage relationships recorded at membrane potentials from -75 mV to $+55$ mV upon 475 nm light activation (power density, 5 mW/mm 2). (D) V_{rev} of C1C2, iC1C2, C1C2_4x, and C1C2_5x [neuronal recording solutions are available in (35)]. (E) Activation spectra of NpHR, C1C2, and iC1C2 measured at power density 0.65 mW/mm 2 for each wavelength and normalized to the maximum amplitude ($n = 6$ cells). (F) V_{rev} of C1C2, iC1C2, C1C2_4x, and C1C2_5x, with internal (int) 120 mM KCl and external (ext) 120 mM NaCl, CsCl, or NaGluconate, pH 7.3 , char-

acterized in HEK cells. (G) As in (A), with ext 120 mM NaCl and int 120 mM KCl, CsCl, or KGluconate, pH 7.3 ($n = 6$ to 17 cells). (H) V_{rev} of iC1C2 under equal (eq) external and internal pH, generating a Nernst potential for protons of 0 mV (dotted green line) at pH 6 and 7.3 . $[Cl^-]_i$ concentration was 8 mM, and $[Cl^-]_o$ was 128 mM, generating a Nernst potential for Cl^- of -71 mV (dotted red line) ($n = 6$ to 9 cells). (I) Current-voltage relationship recorded with equal external and internal pH values at pH 6 and 7.3 ; internal and external $[Cl^-]$ of 8 mM and 128 mM, respectively ($n = 3$ to 8 cells). (J) Photocurrent of iC1C2 at 0 mV from the current-voltage relationship in (I). Error bars indicate SEM.

Fig. 3. Characterization of iC1C2 in mammalian neurons.

(A) Representative photocurrents of C1C2 (left) and iC1C2 (right) recorded at membrane potentials ranging from -80 to 0 mV. 475 nm light (blue bar) was applied at 5 mW/mm 2 . (B) Corresponding current-voltage relationship for photocurrents. (C) V_{rev} of C1C2 and iC1C2 relative to threshold for spike generation (V_{AP}) and to neuron resting potential (V_{rest}) ($n = 8$ to 22 cells). (D) Photocurrent amplitudes (left) and membrane polarization at V_{AP} (right) ($n = 9$ to 14 cells). (E) Mean changes in input resistances were normalized to pre-light value ($n = 9$ to 20 cells). (F) Sample voltage traces of iC1C2-expressing neuron stimulated with varying current injections for 1.5 s, and additional 0.5 s, 475 nm, 5 mW/mm 2 pulses showing effective clamping toward V_{rev} : shown are hyperpolarizing responses below V_{AP} . Error bars indicate SEM.



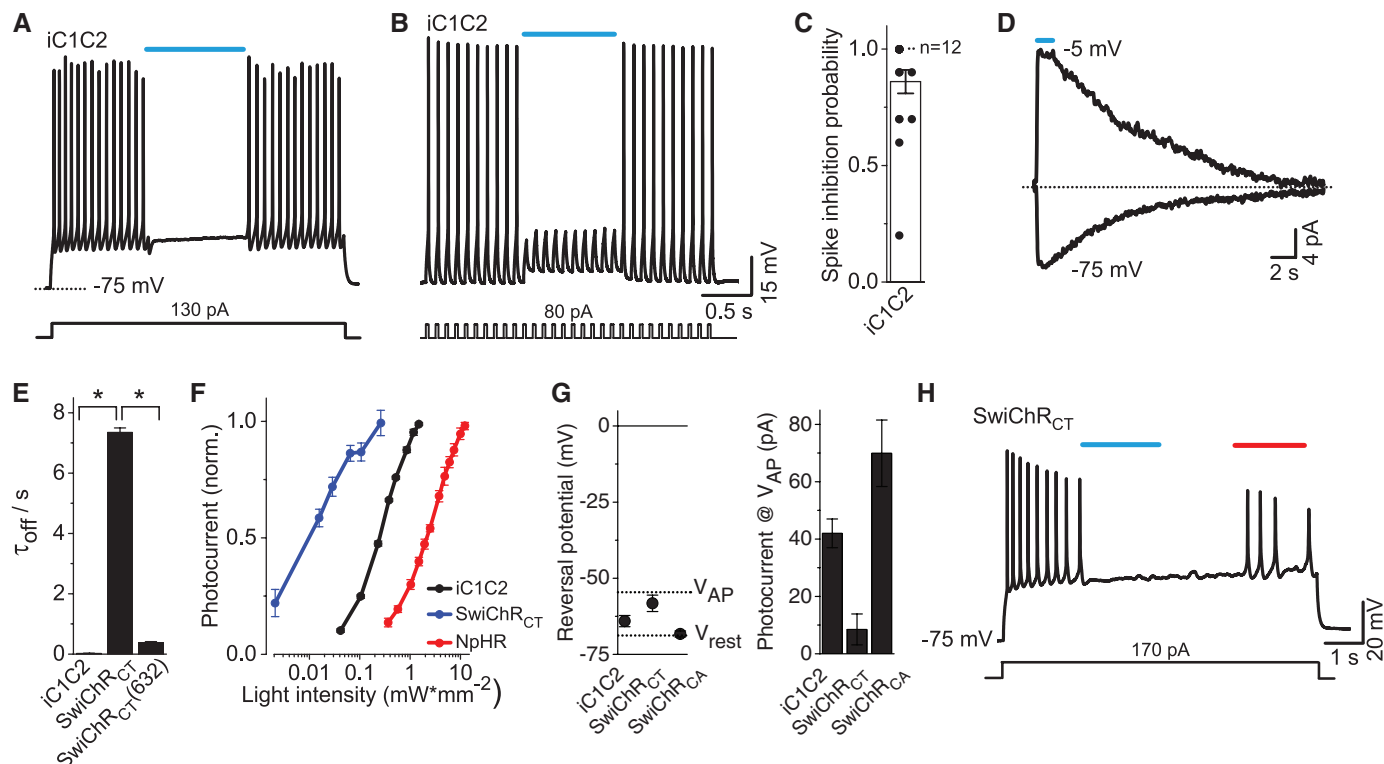


Fig. 4. Fast and bistable inhibition of neuronal spiking with iC1C2 and SwiChR. (A and B) Representative voltage traces of iC1C2-expressing neurons stimulated with either (A) a continuous electrical pulse (3s) or (B) pulsed current injections (10Hz/3s). Electrically evoked spikes were inhibited by 475 nm of light (blue bar) at 5 mW/mm². (C) Distribution of spike-inhibition probability for iC1C2-expressing cells ($n = 18$ neurons; fraction of spikes blocked shown). (D) Inward and outward photocurrents of SwiChR_{CT} in HEK cell upon 475 nm of light (blue bar). (E) Channel off-kinetics (τ) for iC1C2, SwiChR_{CT}, and SwiChR_{CT} exposed to red light during channel closure. (F) Light sensitivity of SwiChR_{CT} compared with that of iC1C2 and NpHR. iC1C2 and SwiChR_{CT} were activated

with 470 nm, and NpHR was activated with 560 nm. Photocurrents were measured at light intensities between 0.0036 and 5 mW/mm², and holding potential was -80 mV. Amplitudes were normalized to the maximum value for each construct ($n = 6$ to 8 cells). (G) Reversal potential of iC1C2, SwiChR_{CT}, and SwiChR_{CA} relative to V_{AP} and V_{rest} ($n = 10$ to 22) (left). Photocurrent amplitudes at V_{AP} are shown at right ($n = 9$ to 15 cells). (H) Bistable spiking modulation by SwiChR_{CT}. Spiking was induced with a continuous electrical pulse (3 s) and stably inhibited with 475 nm light (blue bar). Spiking resumed after 632 nm of light application (red bar). Light power density was 5 mW/mm². Error bars indicate SEM.

stabilized by orders of magnitude after light-off (Fig. 4D). The time-constant of channel closure (τ_{off}) for SwiChR_{CT} was 7.3 s, compared with 24 ms for the parent iC1C2 (Fig. 4E). Beyond stability, another feature of step-function variants is the ability to quickly convert to the closed state upon redshifted light application (21), and indeed, SwiChR_{CT} channel closure was accelerated by application of 632 nm of light (SwiChR_{CT} $\tau_{off-632} = 375$ ms) (Fig. 4E). Another feature of step-function variants is increased light sensitivity of expressing cells, which effectively become photon integrators for long light pulses (23). Indeed, SwiChR_{CT}-expressing cells showed a 25-fold increase in light sensitivity as compared with that of iC1C2, and a 200-fold increase compared with that of the pump-based inhibitor NpHR (Fig. 4F). Similar results were observed in neurons; SwiChR_{CT} generated outward current at AP threshold in neurons with reversal potential of -61 mV and -68 mV for SwiChR_{CA} (Fig. 4G and fig. S3). This sufficed to stably and reversibly inhibit spiking (Fig. 4H and fig. S3) with minimal directly driven current (Fig. 4G and fig. S3) or membrane potential change (Fig. 4H and fig. S3), presenting desirable properties for optogenetic investigation.

We have demonstrated structure-guided conversion of a cation-selective ChR into a light-activated Cl⁻ channel. The iC1C2 mechanism provides more physiological inhibition that does not require a major membrane potential change, and variants enable improvement of stability and light sensitivity by orders of magnitude over existing inhibitory tools. Depolarization-block strategies with excitatory tools (18, 36, 37), although useful in some settings, may not reliably inhibit all targeted cells because light intensities are highly variable in scattering tissue (18, 36–38); in contrast, iC1C2-based tools can only depolarize membranes to V_{rev} of ~ -64 mV (well below V_{AP}) and hyperpolarize when membrane potential is above V_{rev} (Fig. 3F).

Although aspects of final functionality arose by design (for example, removal of acidic residues and introduction of basic residues) (Fig. 2A), other properties remain to be fully explored. For example, iC1C2 showed dependence on external pH; we hypothesize that one or more basic residues within the ion-conducting pathway are protonated and positively charged at physiological and lower external pH, which in turn facilitates association and permeation of anions. Subsequent

improvements in iC1C2 and SwiChR variants by using structure-guided engineering strategies may further enhance photocurrent properties and may be easily ported to complementary and closely related ChR backbones, such as the potent chimeric red (23, 39) and two-photon/infrared (40) light-activated ChRs. The new Cl⁻ permeability of iC1C2 not only provides an unexpectedly effective illustration of cation-channel to anion-channel conversion (41–43) but also demonstrates structure-guided design of ChRs for new classes of functionality.

References and Notes

1. D. Oesterhelt, W. Stoeckenius, *Nat. New Biol.* **233**, 149–152 (1971).
2. A. Matsuno-Yagi, Y. Mukohata, *Biochem. Biophys. Res. Commun.* **78**, 237–243 (1977).
3. G. Nagel et al., *Science* **296**, 2395–2398 (2002).
4. K. Deisseroth, *Nature* **505**, 309–317 (2014).
5. K. Deisseroth, *Nat. Methods* **8**, 26–29 (2011).
6. L. Frenno, O. Yizhar, K. Deisseroth, *Annu. Rev. Neurosci.* **34**, 389–412 (2011).
7. A. M. Packer, B. Roska, M. Häusser, *Nat. Neurosci.* **16**, 805–815 (2013).
8. C. Nonnengässer, E. M. Holland, H. Harz, P. Hegemann, *Biophys. J.* **70**, 932–938 (1996).
9. O. A. Sineshchikov, K. H. Jung, J. L. Spudis, *Proc. Natl. Acad. Sci. U.S.A.* **99**, 8689–8694 (2002).
10. F. Zhang et al., *Cell* **147**, 1446–1457 (2011).

11. E. S. Boyden, F. Zhang, E. Bamberg, G. Nagel, K. Deisseroth, *Nat. Neurosci.* **8**, 1263–1268 (2005).
12. T. Ishizuka, M. Kakuda, R. Araki, H. Yawo, *Neurosci. Res.* **54**, 85–94 (2006).
13. X. Li *et al.*, *Proc. Natl. Acad. Sci. U.S.A.* **102**, 17816–17821 (2005).
14. A. R. Adamantidis, F. Zhang, A. M. Aravanis, K. Deisseroth, L. de Lecea, *Nature* **450**, 420–424 (2007).
15. A. M. Aravanis *et al.*, *J. Neural Eng.* **4**, S143–S156 (2007).
16. A. Berndt, M. Prigge, D. Gradmann, P. Hegemann, *Biophys. J.* **98**, 753–761 (2010).
17. G. Nagel *et al.*, *Proc. Natl. Acad. Sci. U.S.A.* **100**, 13940–13945 (2003).
18. J. Mattis *et al.*, *Nat. Methods* **9**, 159–172 (2012).
19. S. Geibel *et al.*, *Biophys. J.* **81**, 2059–2068 (2001).
20. A. Seki *et al.*, *Biophys. J.* **92**, 2559–2569 (2007).
21. A. Berndt, O. Yizhar, L. A. Gunaydin, P. Hegemann, K. Deisseroth, *Nat. Neurosci.* **12**, 229–234 (2009).
22. C. Bamann, R. Gueta, S. Kleinlogel, G. Nagel, E. Bamberg, *Biochemistry* **49**, 267–278 (2010).
23. O. Yizhar *et al.*, *Nature* **477**, 171–178 (2011).
24. H. E. Kato *et al.*, *Nature* **482**, 369–374 (2012).
25. S. Kleinlogel *et al.*, *Nat. Neurosci.* **14**, 513–518 (2011).
26. D. B. Sauer, W. Zeng, S. Raghunathan, Y. Jiang, *Proc. Natl. Acad. Sci. U.S.A.* **108**, 16634–16639 (2011).
27. B. Roux, R. MacKinnon, *Science* **285**, 100–102 (1999).
28. G. Yellen, *Nature* **419**, 35–42 (2002).
29. M. Köhler *et al.*, *Science* **273**, 1709–1714 (1996).
30. C. M. Nimigeon, J. S. Chappie, C. Miller, *Biochemistry* **42**, 9263–9268 (2003).
31. D. Bichet, M. Grabe, Y. N. Jan, L. Y. Jan, *Proc. Natl. Acad. Sci. U.S.A.* **103**, 14355–14360 (2006).
32. A. Berndt *et al.*, *Proc. Natl. Acad. Sci. U.S.A.* **108**, 7595–7600 (2011).
33. D. E. Clapham, C. Montell, G. Schultz, D. Julius; International Union of Pharmacology, *Pharmacol. Rev.* **55**, 591–596 (2003).
34. Single-letter abbreviations for the amino acid residues are as follows: A, Ala; C, Cys; D, Asp; E, Glu; F, Phe; G, Gly; H, His; I, Ile; K, Lys; L, Leu; M, Met; N, Asn; P, Pro; Q, Gln; R, Arg; S, Ser; T, Thr; V, Val; W, Trp; and Y, Tyr. In the mutants, other amino acids were substituted at certain locations; for example, E136R indicates that glutamic acid at position 136 was replaced by arginine.
35. Materials and methods are available as supplementary materials on Science Online.
36. H. Liske, X. Qian, P. Anikeeva, K. Deisseroth, S. Delp, *Sci. Rep.* **3**, 3110 (2013).
37. A. M. Herman, L. Huang, D. K. Murphey, I. Garcia, B. R. Arenkiel, *eLife* **3**, e01481 (2014).
38. Y. Andrews-Zwilling *et al.*, *PLOS ONE* **7**, e40555 (2012).
39. J. Y. Lin, P. M. Knutsen, A. Muller, D. Kleinfeld, R. Y. Tsien, *Nat. Neurosci.* **16**, 1499–1508 (2013).
40. R. Prakash *et al.*, *Nat. Methods* **9**, 1171–1179 (2012).
41. J. L. Galzi *et al.*, *Nature* **359**, 500–505 (1992).
42. M. J. Gunthorpe, S. C. Lummis, *J. Biol. Chem.* **276**, 10977–10983 (2001).
43. H. Yang *et al.*, *Cell* **151**, 111–122 (2012).

Acknowledgments: We thank C. Perry and H. Swanson for technical assistance, the entire Deisseroth laboratory for helpful discussions, and T. Jardtzy for use of a Biotek Synergy4 plate reader. K.D. is supported by the National Institute of Mental Health, the Simons Foundation Autism Research Initiative, the National Institute on Drug Abuse, the Defense Advanced Research Projects Agency, the Gatsby Charitable Foundation, and the Wiegers Family Fund. A.B. received support from the German Academic Exchange Service (DAAD), and S.Y.L. received support from the Fidelity Foundation. Optogenetic tools and methods reported in this paper are distributed and supported freely (www.optogenetics.org).

Supplementary Materials

www.sciencemag.org/content/344/6182/420/suppl/DC1
Materials and Methods
Figs. S1 to S3

18 February 2014; accepted 19 March 2014
10.1126/science.1252367

Neural Mechanisms of Object-Based Attention

Daniel Baldauf* and Robert Desimone

How we attend to objects and their features that cannot be separated by location is not understood. We presented two temporally and spatially overlapping streams of objects, faces versus houses, and used magnetoencephalography and functional magnetic resonance imaging to separate neuronal responses to attended and unattended objects. Attention to faces versus houses enhanced the sensory responses in the fusiform face area (FFA) and parahippocampal place area (PPA), respectively. The increases in sensory responses were accompanied by induced gamma synchrony between the inferior frontal junction, IFJ, and either FFA or PPA, depending on which object was attended. The IFJ appeared to be the driver of the synchrony, as gamma phases were advanced by 20 ms in IFJ compared to FFA or PPA. Thus, the IFJ may direct the flow of visual processing during object-based attention, at least in part through coupled oscillations with specialized areas such as FFA and PPA.

When covertly attending to a location in the periphery, visual processing is biased toward the attended location, and the sources of top-down signals include the frontal eye fields (FEF) (1, 2) and parietal cortex (PC). FEF may modulate visual processing through a combination of firing rates and gamma frequency synchrony with visual cortex (2). For nonspatial attention, the mechanisms of top-down attention are much less clear. When people attend to a feature, such as a particular color (3–5), or to one of several objects at the same location (6–8), activity in the extrastriate areas representing properties of the attended object is enhanced. But where do the attentional biases (9) come from, and how do they enhance object processing when the distractors are not spatially separate?

We combined magnetoencephalography (MEG), supplemented by functional magnetic resonance imaging (fMRI) and diffusion tensor

imaging to optimize both spatial and temporal resolution. In the MEG experiment, two spatially overlapping streams of objects (faces and houses) were tagged at different presentation frequencies (1.5 and 2.0 Hz) (Fig. 1, A and B) (5, 10–12). The stimuli went in and out of “phase coherence,” so that they were modulated in visibility over time but did not change in luminance or flash on and off. When subjects were cued to attend to one of the streams and to detect occasional targets within the cued stream, frequency analyses allowed identifying brain regions that followed the stimulus oscillations.

Using MEG data only (13), the strongest activity evoked by the face tag was in the right fusiform gyrus, whereas the activity evoked by the house tag was more medially in the inferior-temporal cortex (IT) (Fig. 1C; figs. S1 and 2 for individual subjects and alternative source reconstruction approaches). These areas were roughly consistent with the locations of fusiform face area (FFA) and parahippocampal place area (PPA) determined previously in fMRI (14–16). To increase the accuracy of localization in each sub-

ject, we added high-resolution fMRI localizers for FFA and PPA (Fig. 2, B and D, and fig. S3A), which were focused at the expected spots (Fig. 2F).

To identify other areas important for nonspatial attention, we contrasted the brain state when attending to one of the two superimposed object classes with a similarly demanding state that did not require attending to either object class. The attention-related fMRI localizers revealed consistent activation in the inferior frontal junction (IFJ) at the intersection of the inferior-frontal and precentral sulcus (17–19) (Fig. 2, A, C, and E), with weaker and less-consistent signals in posterior-parietal and in inferior-temporal cortex (fig. S3C). A control experiment confirmed that IFJ’s activation was indeed related to nonspatial attention, rather than simply memory (fig. S4).

Each subject’s individual fMRI localizers were then used as regions of interest (ROIs) to guide the analysis of the MEG signals (see supplementary material for a description of the coregistration of fMRI and MEG). The modulation of sensory responses by attention in the tagging-frequency range is shown in Fig. 2G (fig. S5B for individual subjects). FFA and PPA had the strongest responses, with FFA more responsive to the attended face tag (*t* test, $P < 0.001$) and PPA more responsive to the attended house tag (*t* test, $P < 0.01$). Thus, object-specific attention modulates the sensory responses in FFA and PPA. Weaker sensory responses were found in region V1.

Although weaker in amplitude, sensory responses were also found in IFJ, and the attention effects were much stronger—there was a tagging frequency response only to the attended object (both *t* test, $P < 0.001$). Control regions in the FEF (localized in separate fMRI runs, fig. S3D), PC (localized in the attention-related fMRI experiment in some participants) and the frontal pole (anatomically defined) showed only minor and less consistent responses. The general pattern of

McGovern Institute for Brain Research, Massachusetts Institute of Technology, Cambridge, 02139 MA, USA.

*Corresponding author. E-mail: baldauf@mit.edu